Citation (APA)
Petallidou, K. C., Gounaris, D., Ternero, P., Messing, M. E., Schmidt-Ott, A., & Biskos, G. (2026). Synthesis of metal nitride and metal oxide nanoparticles by atmospheric-pressure spark ablation. *Journal of Materials Chemistry C*, *14*(9), 3629-3636. https://doi.org/10.1039/d5tc02874d

Acta Materialia 309 (2026) 122061

Contents lists available at ScienceDirect

Acta Materialia

journal homepage: www.elsevier.com/locate/actamat

Full length article

Revealing atomic structure and chemical complexity of vanadium carbide nanoprecipitates in microalloyed steels

Amir Sabet Ghorabaei [a,*], Maria Giuseppina Mecozzi [b], Zamran Zahoor Khan [c], Majid Ahmadi [a], Steven R. Parnell [c], Sven Erik Offerman [b], Niels H. van Dijk [c], Bart J. Kooi [a,*]

[a] Zernike Institute for Advanced Materials, University of Groningen, Nijenborgh 3, 9747 AG Groningen, The Netherlands
[b] Department of Materials Science and Engineering, Delft University of Technology, Mekelweg 2, 2628 CD Delft, The Netherlands
[c] Department of Radiation Science and Technology, Delft University of Technology, Mekelweg 15, 2629 JB Delft, The Netherlands

ARTICLE INFO

Keywords:
Precipitation mechanisms
Scanning transmission electron microscopy
Small-angle neutron scattering
Solute-drag effect
Microalloyed steels

ABSTRACT

Microalloyed low-carbon steels strengthened by vanadium carbide (VC) nanoprecipitates are receiving increasing attention, particularly in the automotive industry. A clear understanding of the nanoprecipitate chemistry is essential for optimizing the alloy composition and processing routes, thereby enhancing the mechanical properties of such advanced steels. The chemical evolution of VC precipitates, especially regarding the incorporation of iron into the nanoprecipitates, remains uncertain. Here, a model vanadium-microalloyed low-carbon steel is studied by atomic-resolution scanning transmission electron microscopy (STEM) techniques. The steel contains nanoscale VC precipitates formed either as interphase precipitates (IP) at the austenite/ferrite interface during the austenite-to-ferrite phase transformation, or as randomly distributed precipitates (RP) in the ferrite matrix during bainite tempering. The first-time observation of carbon sublattice atoms in VC is achieved using integrated differential phase-contrast STEM (iDPC-STEM). Non-equilibrium compositions are identified under both precipitation mechanisms, with no correlation between precipitate size and associated elemental contents. Most interphase VC nanoprecipitates contain higher amounts of not only iron but also manganese compared to random VC nanoprecipitates. Complementary ex-situ small-angle neutron scattering (SANS) analysis and solute-drag effect (SDE) modeling support the co-segregation of iron and manganese into the precipitates. Manganese typically appears to form a core–shell-like structure within VC. Experimental evidence is presented for the SDE-assisted formation of manganese-rich-core (fibrous) interphase VC precipitates, and a mechanism is proposed for iron–manganese co-enrichment in random VC precipitates. This study offers new insights into future strategies to tune nanoprecipitate chemistry in microalloyed steels.

1. Introduction

The demand for lightweight, resource-efficient, yet high-performance steels has led to the development of advanced micro-alloyed nano-steels [1,2]. These alloys typically contain small amounts (usually below 0.5 wt.%) of vanadium, titanium, niobium, and/or molybdenum, which, under appropriate heat treatment conditions, react with dissolved carbon in the iron matrix to form a dispersion of nanoscale carbides, such as vanadium carbide (VC) [3,4], titanium carbide (TiC) [5,6], niobium carbide (NbC) [7,8], molybdenum carbide (MoC) [9,10], or multi-component carbides [11–16]. These nanoprecipitates form either through the interphase precipitation (IP) mechanism during the austenite-to-ferrite phase transformation [17–20] or through the so-called random precipitation (RP) mechanism that becomes effective after quenching and aging a prior austenitic matrix [21–24]. Understanding the chemistry of such nanoprecipitates is critically important, as it not only correlates with the driving force and thus the kinetics of precipitation (as reflected in the precipitate volume fraction, size distribution, number density, and morphology) but also influences the mechanical response of the precipitate-containing material (as manifested through precipitation strengthening mechanisms) [25–27].

Several studies have demonstrated variations in the chemical composition of nanoprecipitates during precipitation reactions in microalloyed steels [13,23,28–33]. In a titanium–molybdenum

---

* Corresponding authors.
E-mail addresses: amir.sabet.ghorabaei@rug.nl (A. Sabet Ghorabaei), b.j.kooi@rug.nl (B.J. Kooi).

https://doi.org/10.1016/j.actamat.2026.122061
Received 10 December 2025; Received in revised form 14 February 2026; Accepted 25 February 2026

microalloyed low-carbon steel, the sublattice fractions of molybdenum and iron decreased with increasing the (Ti,Mo,Fe)C precipitate size in the austenite phase [13]. In contrast, during interphase (Ti,Mo,Fe)C precipitation in a similar microalloyed steel, the Mo/Ti atomic ratio within the precipitates indicated a slight increase with increasing precipitate size [30]. In a titanium–vanadium microalloyed low-carbon steel, the site fraction of titanium in random-precipitated (Ti,V)C decreased continuously during the precipitate growth within the ferrite phase, which was attributed to the difference in the diffusion coefficients of solute titanium and vanadium atoms [23]. Interestingly, atom-probe tomography (APT) measurements on interphase (Ti,Mo)C nanoprecipitates revealed no correlation between precipitate size and corresponding constituent element contents [31]. However, in another study on titanium and titanium–molybdenum microalloyed steels, APT measurements showed high atomic fractions of iron (70–85 at.%) in the core of the interphase TiC and (Ti,Mo)C precipitates [33]. Similar iron contents were also reported for APT measurements on interphase (Nb, Fe)C precipitates in a niobium-microalloyed low-carbon steel [28]. These precipitates were interpreted as metastable carbides, and the presence of iron was thought to ease the nucleation by lowering the required activation energy through a reduction in the precipitate–matrix lattice misfit. Nevertheless, distinguishing solute levels in the matrix from those in the nanoprecipitates using APT is generally complex [30, 34–36].

Regarding the incorporation of iron in the structure of VC nanoprecipitates in vanadium-microalloyed steels, earlier electron microscopy studies indicated that the presence of a relatively high iron content in interphase VC precipitates was a result of poor carbon extraction replica (CER) preparation, suggesting that iron residues (possibly in form of a coating layer) from the matrix etching participated in the measured high apparent iron content in the precipitates [37]. A recent in-situ small-angle neutron scattering (SANS) study on a vanadium-microalloyed steel reported a gradual evolution of the precipitate composition with the precipitate size, consistent with a high iron concentration during the early stages of the interphase VC precipitation, followed by a gradual reduction in the iron content toward the orthoequilibrium concentration [27]. The APT measurements in that study were only focused on isothermal aging time intervals far beyond the end of the austenite-to-ferrite phase transformation, limiting the information on the chemical composition of VC at earlier interphase precipitation stages [27]. Furthermore, recent preliminary studies have demonstrated signs of a lower concentration of iron within random-precipitated VC in a (tempered) bainitic matrix compared to interphase-precipitated VC in a ferritic matrix [38,39]. These divergent perspectives in combination with the lack of data on the chemical composition of random-precipitated VC necessitate a more in-depth and direct study of the chemistry of VC nanoprecipitates to further understand the influence of solute alloying elements on the formation of these nanoscale precipitates in the interphase and random precipitation mechanisms.

Here, the chemical composition of nanoscale interphase- and random-precipitated vanadium carbide is systematically studied in a microalloyed low-carbon steel with predominantly ferritic and bainitic microstructures aiming to: (1) investigate whether iron is present within the nanoprecipitates and whether its internal concentration is spatially uniform; (2) find any correlation between the precipitate size and the elemental concentrations; (3) establish whether manganese enrichment also occurs within the precipitates; and (4) propose mechanisms responsible for compositional variations in the precipitates. To this end, atomic-resolution scanning transmission electron microscopy (STEM) techniques are complemented by an analysis of SANS data and solute-drag effect (SDE) modeling to unravel the atomic structure and chemistry of VC nanoprecipitates.

2. Methods

2.1. Material and heat treatments

A low-carbon low-vanadium (LCLV) Fe–C–Mn–V model steel, produced by Tata Steel (IJmuiden, The Netherlands), was used in this study. Table 1 shows the chemical composition of the alloy, featuring a 1:1 atomic ratio of V:C. Samples with dimensions of 11 × 11 × 1 mm^3 were cut from the as-received 3 mm-thick hot-rolled plate and heat treated in a TA Instruments DIL 850A/D dilatometer equipped with an induction heating system (see Supplementary Information, Fig. S1). The samples were first heated to an austenitization temperature of 1050 °C with a heating rate of 5 °C s^{-1} and held at this temperature for 15 min in a vacuum of about 10^{-4} mbar. The austenitization temperature was above the orthoequilibrium austenite-finish temperature ($A_3 = 830$ °C) and the dissolution temperature of *M*C-type precipitates ($T_D = 990$ °C) according to Thermo-Calc calculations [40]. Subsequently, the austenitized sample was cooled down with a rate of 15 °C s^{-1} by helium gas to 650 °C and isothermally heat treated for 20 min (until the end of the austenite-to-ferrite phase transformation [38,40,41]), followed by cooling to room temperature to produce a predominantly ferritic microstructure with interphase nanoprecipitates (marked as the LCLV-IP samples). Another austenitized sample was first cooled down with the same cooling rate to room temperature to produce a bainitic microstructure during continuous cooling [38], followed by an isothermal heat treatment at 650 °C for 20 min to promote the formation of random nanoprecipitates within bainitic ferrite laths (marked as the LCLV-RP samples). Typical optical micrographs from the microstructures of the heat-treated samples are shown in Fig. S2.

2.2. STEM procedure

Samples for electron microscopy were prepared by using an optimized direct CER preparation method [38]. The heat-treated samples were first metallographically prepared in accordance with the ASTM E3–11 standard, with final polishing using a 250 nm diamond suspension. Then, the freshly polished surfaces of the samples were lightly etched with a 2% Nital etchant (2 vol.% HNO_3 + 98 vol.% C_2H_5OH) for 5 s, followed by back-polishing and re-etching with the same conditions. The samples were subsequently rinsed with distilled water, isopropyl alcohol, and then were dried with compressed air. Freshly etched surfaces of the samples were coated with an 8 ± 2 nm-thick amorphous carbon film in a vacuum of 3 × 10^{-6} mbar by using an Edwards E306A thermal evaporator coating system. The coated samples were kept in ambient conditions for about 24 h and then about 2 × 2 mm^2 regions were scribed on the coated surfaces of the samples. The scribed carbon films were stripped by using a water-based stripping solution consisting of 2 vol.% HNO_3 + 5 vol.% C_2H_5OH + 93 vol.% distilled H_2O. Afterward, a water-based cleaning solution consisting of 5 vol.% C_2H_5OH + 95 vol.% distilled H_2O was used to clean the CERs for six times. Substrate-free copper TEM grids with a 300 square mesh were used to collect the CERs from the cleaning solution. The prepared TEM grids were dried by using infrared light, ready for electron microscopy observations.

Overall screening of the CERs and microstructural observation of nanoprecipitates were carried out by high-angle annular dark-field STEM (HAADF-STEM) with an FEI Helios G5 CX dual-beam FIB-SEM (focused ion beam-scanning electron microscope) operating at an accelerating voltage of 30 kV and a beam current of 0.17 nA. Detailed HAADF-STEM imaging was performed by a TFS Titan Themis Z probe- and image-aberration–corrected S/TEM equipped with a Dual-X energy-dispersive X-ray spectroscopy (EDS) detector at an accelerating voltage of 300 kV, a convergence semi-angle of 18.0 mrad, and a probe current of about 150 pA. Atomic-resolution HAADF-STEM imaging was conducted using a probe current of about 25 pA and a HAADF detector collection angle range of 43–200 mrad at a camera length of 115 mm.

Table 1
Chemical composition of the studied steel in wt.% (at.%).

C	Mn	V	Si	S	P	Fe
0.071 (0.329)	1.84 (1.86)	0.29 (0.32)	0.01 (0.02)	0.0016 (0.0028)	0.0010 (0.0018)	Balance

Moreover, a recently developed integrated differential phase-contrast STEM (iDPC-STEM) technique [42] was implemented to reveal both heavy and light constituent elements of *M*C-type nanoprecipitates in atomic-resolution for the first time. The workflow of the iDPC technique is illustrated in Fig. S3. iDPC-STEM images were acquired at a probe current of about 25 pA by a segmented DPC detector with a collection angle range of 5–20 mrad at a camera length of 235 mm. Standard high-pass Gaussian filtering with a size of 10 px was applied to iDPC-STEM images in Velox S/TEM data acquisition and processing software for removing carbon contamination effects [43]. For validation of experimental atomic-resolution HAADF-STEM and iDPC-STEM images, corresponding multislice STEM image simulations were performed before the experiments by Dr. Probe software [44] in combination with in-house written MATLAB scripts [43]. The rock salt crystal structure ($Fm\overline{3}m$ space group) of *M*C-type nanoprecipitates was manipulated and prepared for the simulations in VESTA [45] and Dr. Probe software packages (see Fig. S4). The simulation parameters were chosen close to the experimental values as provided in Table S1.

Quantitative chemical analyses of nanoprecipitates were performed by STEM-EDS spectrum imaging (STEM-EDS SI) at a probe current of about 500 pA. Typical STEM-EDS SI acquisition and processing parameters that were used in this study are provided in Table S2. Approximately 20 STEM-EDS SI datasets were acquired for each sample. After initial X-ray background subtraction, X-ray peaks fitting, and pre- and post-filtering for all spectrum images, the spectra of about 200 nanoprecipitates for each sample were individually isolated from those of the surrounding carbon replicas in a manual procedure (see Fig. S5). The standardless Cliff-Lorimer method without absorption correction was used for the quantification of isolated STEM-EDS SI spectra considering only K_α radiation of elements of interest (i.e., V, Fe, and Mn, excluding C). The chemical formula of nanoprecipitates is represented as $Fe_xMn_zV_{1-x-z}C_y$, where *x, y*, and *z* are expressed as the atomic site fractions.

2.3. SANS analysis

Room-temperature SANS measurements were performed on the heat-treated samples [39] to obtain the scattered intensity ($\partial\Sigma/\partial\Omega$) as a function of the wave-vector transfer $Q = 4\pi\sin(\theta)/\lambda$, where λ is the neutron wavelength and θ is half of the scattering angle. An external magnetic field of 1.5 T was applied to the samples during the measurements to allow the separation of the two scattering components, namely the nuclear and the magnetic scattering. Following the developed method in a previous study [27], the composition of nanoprecipitates, with the chemical formula $Fe_xMn_zV_{1-x-z}C_y$, can be calculated from the so-called *A*-factor, which is the ratio of the nuclear and the magnetic scattering from the same distribution of precipitates:

$$A = \frac{\left(\frac{\partial\Sigma}{\partial\Omega}\right)_{nuc}}{\left(\frac{\partial\Sigma}{\partial\Omega}\right)_{mag}} = \frac{\Delta\rho^2{}_{nuc}}{\Delta\rho^2{}_{mag}} = \frac{\left(\frac{(1-z_{matrix})\cdot b_{Fe} + z_{matrix}\cdot b_{Mn}}{V_{matrix}} - \frac{x\cdot b_{Fe} + (1-x-z)\cdot b_V + z\cdot b_{Mn} + y\cdot b_C}{V_{prec}}\right)^2}{\Delta\rho^2{}_{mag}} = f(x,y,z) \tag{1}$$

In Eq. (1), $\Delta\rho^2{}_{nuc}$ and $\Delta\rho^2{}_{mag}$ are estimated nuclear and magnetic contrasts, respectively. Constants b_V, b_{Fe}, b_{Mn}, and b_C are coherent scattering lengths of vanadium, iron, manganese, and carbon, which correspond to -0.3824×10^{-15}, 9.45×10^{-15}, -3.73×10^{-15}, and 6.646×10^{-15} m, respectively. Variables *x*, *z*, and *y* are site fractions of iron, manganese, and carbon in the nanoprecipitates; z_{matrix} is the site fraction of manganese in the matrix, which is assumed to be equal to the nominal manganese site fraction of the alloy. $\Delta\rho^2{}_{mag}$ represents the magnetic contrast between the ferromagnetic iron matrix and the paramagnetic VC precipitate phase [46]. The iron matrix is magnetically ordered, and its magnetic moments can be aligned under an applied magnetic field of 1.5 T. In contrast, the VC precipitates, which may incorporate a limited amount of iron, are magnetically disordered. As a result, the applied magnetic field of 1.5 T is insufficient to align their magnetic moments, effectively rendering them non-magnetic under these conditions. $\Delta\rho^2{}_{mag}$ was estimated to be 24.59×10^{28} m^{-4} [39]. V_{matrix} and V_{prec} are the atomic volumes of the iron matrix and the precipitate, respectively. They were calculated as $V_{matrix} = a^3_{matrix}/2$ and $V_{prec} = a^3_{prec}/4$, where $a_{matrix} = 0.287$ nm and $a_{prec} = 0.417$ nm are the corresponding lattice parameters of the unit cell in the matrix and in the precipitate, respectively. The unit cell of the matrix contains $Z = 2$ formula units, and the unit cell of the VC precipitate contains $Z = 4$ formula units. Two modifications were made to Eq. (1) in comparison with the previous study [27]. First, the manganese site fraction in the precipitates, *z*, was taken to be a variable. Second, the VC precipitates were assumed to exhibit non-magnetic behavior. The variations in the *A*-factor in compositional space were evaluated by sequentially varying the three independent components within the precipitates (i.e., Fe, Mn, and C). Moreover, using the mean of experimental *A*-factor value for each sample [39], the compositional space of $Fe_xMn_zV_{1-x-z}C_y$ nanoprecipitates was calculated as a function of iron and manganese site fractions for fixed values of carbon site fraction.

2.4. Solute-drag model for interphase precipitation

To evaluate the segregation tendency of manganese at moving ferrite/austenite (α/γ) interfaces and its correlation to the chemical complexity of interphase nanoprecipitates, the solute-drag model proposed by Miyamoto and coworkers [47] for a ternary alloy is modified here to apply to the quaternary Fe–C–Mn–V system relevant to this study. Following the treatment by Hillert and Sundman [48], the Gibbs free energy dissipation due to the SDE of the element *i*, ΔG^i_{SDE} [J mol^{-1}], is expressed as:

$$\Delta G^i_{SDE} = -\frac{V_m}{\nu}\int_{-\delta}^{\delta} J_i \frac{d\Delta\mu_i}{dX}\,dX \tag{2}$$

In Eq. (2), V_m is the molar volume of the matrix, ν is the α/γ interface velocity, δ is half the width of the α/γ interface, J_i is the diffusion flux of the substitutional element i, $\Delta\mu_i$ is the diffusion potential of the substitutional element i ($\Delta\mu_i = \mu_i - \mu_{Fe}$), and X is the spatial coordinate with the origin at the center of the diffuse α/γ interface. The driving force for interdiffusion of the element i within the α/γ interface is represented by $d\Delta\mu_i/dX$ in Eq. (2). The regular solution model was used to describe the thermodynamics of the system, assuming random mixing of components occupying a specific sublattice [49]. The diffusion flux of the element i in Eq. (2) is given by Eq. (3) [47] as follows:

$$J_i = -\frac{D_i}{RTV_m} y_{Fe} y_i \frac{d\Delta\mu_i}{dX} \tag{3}$$

where D_i is the trans-interface diffusivity of the element i in the α/γ interface, $y_i = x_i/(1 - x_C)$ is the site fraction of element i (with x_i atomic fraction) in the V–Fe–Mn sublattice, R is the gas constant, and T is temperature in kelvin. The diffusion potential of the element i is given by Eq. (4) [47] as follows:

$$\Delta\mu_i = G_i^0 + RT\varepsilon_{i,C} y_C + RTln\frac{y_i}{y_{Fe}} + E_i(X) \tag{4}$$

where G_i^0 is the free energy of one mole of pure element i, $\varepsilon_{i,C}$ is the Wagner interaction parameter between the element i and carbon, and $E_i(X)$ is a triangular-shaped potential well within the α/γ interface of finite width 2δ, used to describe the interaction between the solutes and the moving α/γ interface (see Fig. S6).

Assuming steady-state conditions for each component at the α/γ interface, the following equation must be fulfilled for carbon, manganese, and vanadium [47]:

$$\frac{\partial}{\partial X}(vy_i - V_m J_i) = 0 \tag{5}$$

Solving the system of differential equations derived from Eq. (5) enables the determination of the concentration profiles of the alloying elements within the diffuse α/γ interface as a function of the interface velocity. ΔG_{SDE}^{Mn} and ΔG_{SDE}^{V} are subsequently derived from the corresponding concentration profiles using Eq. (2). The excess site fraction of manganese or vanadium within the α/γ interface is given by Eq. (6) as follows:

$$\Delta y_i = \frac{1}{2\delta}\int_{-\delta}^{+\delta}\left(y_i - y_i^0\right)dX \tag{6}$$

where y_i^0 is the site fraction of the element i in ferrite. The parameters of the SDE model are listed in Table S3, and additional details of the model are provided in [47].

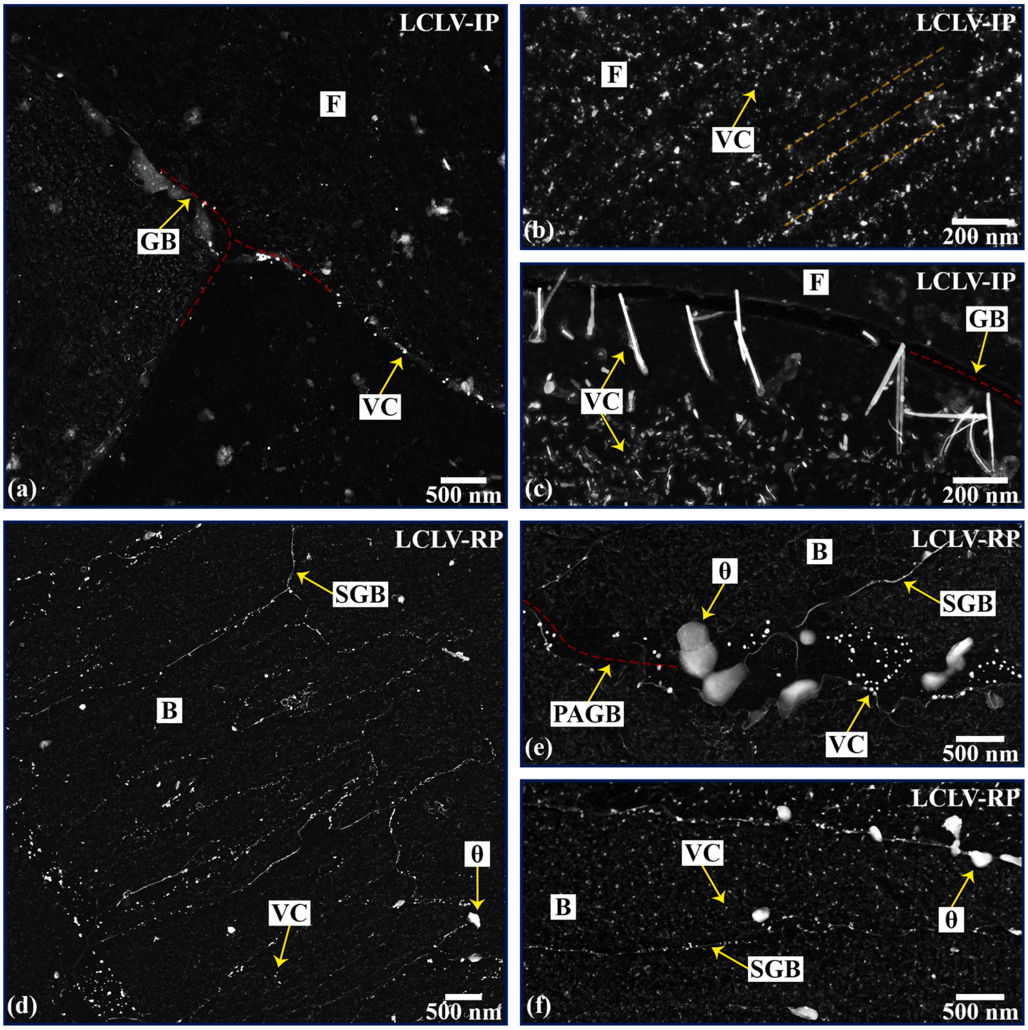

Fig. 1. Spatial distribution and morphology of precipitates on CERs. (a–c) and **(d–f)** HAADF-STEM images illustrating precipitates in the replicated ferritic and bainitic microstructures of the LCLV-IP and LCLV-RP samples, respectively. F: ferrite, B: bainite, VC: vanadium carbide, θ: cementite, GB: grain boundary, SGB: subgrain boundary, PAGB: prior austenite grain boundary.

3. Results

3.1. Spatial distribution and morphology of precipitates

Fig. 1(a–c) represent typical HAADF-STEM images of nanoprecipitates from the LCLV-IP CERs. The results demonstrate that the grain boundaries of ferrite are sparsely decorated with relatively coarse VC precipitates (Fig. 1(a)). Interphase VC precipitates, with their characteristic sheet-like morphology, are randomly observed in some regions of the CERs (Fig. 1(b)). Moreover, fibrous VC precipitates are identified near the grain boundaries of several ferrite grains (Fig. 1(c)). These precipitates are oriented almost perpendicular to the ferrite (prior ferrite/austenite) grain boundaries and are associated with a precipitation-free interface zone in their vicinity, supporting earlier observations on the microstructural evolution of fibrous VC nanoprecipitates [9,50–52]. Additionally, randomly distributed VC precipitates are observed within various ferrite grains (Fig. 1(c)). These precipitates could either be interphase VC in nature, replicated from a non-ideal orientation during CER preparation, or they could be random VC precipitates formed within certain ferrite grains. There is strong experimental evidence that not all ferrite grains contain interphase VC precipitates due to the lack of proper orientation relationships with prior austenite grains during interphase precipitation [20,53,54], which can result in the formation of random VC precipitates within the ferrite grains (Fig. 1(a) and (c)).

Fig. 1(d–F) show typical HAADF-STEM images of nanoprecipitates from the LCLV-RP CERs. The formation of VC nanoprecipitates in the LCLV-RP sample frequently occurs at subgrain boundaries of bainitic ferrite and at prior austenite grain boundaries (Fig. 1(d) and (e)). However, finer VC precipitates are also observed within bainitic ferrite laths (Fig. 1(f)). Moreover, relatively large (sub)grain boundary cementite particles, associated with the bainite formation, are identified in the microstructure (Fig. 1(d–F)). Whereas the fibrous morphology of VC is observed only in the LCLV-IP sample, other morphologies—-spherical, ellipsoidal, and irregular—are present in both samples. The average VC precipitate sizes reported from previous TEM work [38] are 4.8 ± 3.0 nm and 6.9 ± 6.5 nm for the LCLV-IP and LCLV-RP samples, respectively. The corresponding VC volume fractions reported from prior SANS measurements [39] are 0.35% ± 0.09% and 0.19% ± 0.04%, both below the orthoequilibrium value of 0.56% at 650 °C calculated using Thermo-Calc software (version 2023b) with the TCFE12 database [55].

3.2. Atomic-resolution electron microscopy of VC

A HAADF-STEM image along the $\langle 110\rangle$ zone axis of a grain-boundary precipitated VC is shown in Fig. 2(a). This ellipsoidal VC nanoprecipitate is elongated along the $\langle 100\rangle$ crystallographic direction with $\langle 011\rangle$ sidewise growth directions. The atomic-resolution structure of this nanoprecipitate (from the indicated region in Fig. 2(a)) is presented by both HAADF-STEM and iDPC-STEM images in Fig. 2(b) and (c), respectively. Comparing the HAADF and iDPC images, the latter clearly reveals the C sublattice atoms alongside the *M* (i.e., V, Fe, and Mn) sublattice atoms. This first-time observation of carbon sublattice atoms in VC is validated by atomic-resolution iDPC imaging of VC nanoprecipitates along other low-index zone axes of $\langle 100\rangle$, $\langle 111\rangle$, and $\langle 211\rangle$, where carbon atomic columns can also be resolved when observing the nanoprecipitates along the $\langle 211\rangle$ zone axis (see Fig. S7).

HAADF-STEM and iDPC-STEM image simulations were carried out for the evaluation of corresponding experimental images, particularly with the aim of assessing the feasibility of distinguishing vanadium atoms from other *M*-type elements (specifically iron atoms) in the nanoprecipitates. Fig. 2(d–i) show experimental HAADF and iDPC images (from the indicated regions in Fig. 2(b) and (c)) in combination with image intensity profile analyses across the atomic columns. Fig. 2 (j–o) depict the simulation results for an iron-doped VC crystal with a stoichiometry of $Fe_{0.125}V_{0.875}C$ and with a thickness of 10 nm along the [110] zone axis. Alternating atomic layers of iron and vanadium were considered along this zone axis at specific lattice sites (Fig. S4). Under these conditions, the mixed iron–vanadium atomic columns produce about 14% more HAADF detector intensity (approximately scaling with the square of the atomic number) compared to that of the pure vanadium atomic columns. These observations suggest that the atomic-resolution imaging of iron atoms at such a doping level within the nanoprecipitates is only possible if the iron forms an ordered sublattice within the crystal structure of VC. However, the iron (and possibly manganese) atoms are expected to be randomly distributed within the VC crystal, individually substituting for vanadium in the corresponding sublattice, which makes it impossible to distinguish the constituent elements (Fig. 2(i)). Nevertheless, atomic-scale STEM-EDS SI could reveal the iron and manganese distribution within the nanoprecipitates (see Section 3.3). It is worth mentioning that the iDPC detector intensity (approximately scaling linearly with the atomic number) indicates simulation artifacts because the relative intensity value of the iron–vanadium atomic columns (with a higher effective atomic number) is lower (–9% in Fig. 2(n)) than that of the pure vanadium atomic columns (with a lower effective atomic number). Furthermore, experimental iDPC images reveal a lower relative intensity difference between carbon and *M*-type atoms (–35% in Fig. 2(h)) in comparison to that of the simulation results (–49% in Fig. 2(n)). These discrepancies can partly be attributed to the higher sensitivity of the iDPC-STEM technique to variations in specimen thickness and imaging conditions, particularly electron-beam defocus, compared to the HAADF-STEM technique [42], potentially causing intensity modulations of the atomic columns (see Fig. S9 and S10).

3.3. Statistical spectrum image analysis of VC

Fig. 3 shows the quantitative STEM-EDS SI results of iron and manganese atomic concentrations (equal to site fractions) within the Fe–Mn–V sublattice of VC nanoprecipitates of varying sizes in the LCLV-IP and LCLV-RP CERs, where precipitate size is defined as the largest dimension of individual nanoprecipitates measured from the corresponding HAADF-STEM images. A larger scatter is observed in the data for the LCLV-IP CER compared to the data for the LCLV-RP CER, with no discernible correlation between precipitate size and the corresponding iron or manganese concentration. Both iron and manganese are detected in the VC nanoprecipitates of the two samples, where the iron concentration is generally higher than the manganese concentration. The VC precipitates in the LCLV-IP CER show higher iron and manganese concentrations compared to those in the LCLV-RP CER (Fig. 3(c–F)). In addition, fibrous VC nanoprecipitates are found to contain higher manganese concentrations than most of the VC precipitates with other morphologies. For both samples, the measured iron site fraction for various VC precipitates is predominantly below the orthoequilibrium value of $x_{\text{eq.}} = 0.156$ at 650 °C. Conversely, the measured manganese site fraction is above the orthoequilibrium value of $z_{\text{eq.}} = 0.006$ at 650 °C. Fig. 4 represents the scatter plots from Fig. 3 as frequency-concentration histograms, along with their relevant statistical values. Based on the average iron and manganese concentrations in the VC nanoprecipitates, the corresponding chemical formulas of VC for the LCLV-IP and LCLV-RP samples are $Fe_{0.053}Mn_{0.024}V_{0.923}C_y$ and $Fe_{0.023}Mn_{0.012}V_{0.965}C_y$, respectively.

Typical elemental maps derived from the STEM-EDS SI data of VC nanoprecipitates for the LCLV-IP and LCLV-RP samples are illustrated in Fig. 5. According to the quantitative EDS spectrum profile analysis for ellipsoidal and fibrous VC nanoprecipitates in the LCLV-IP sample, the core of the precipitates is enriched in manganese (Fig. 5(e) and (j)). This observation is particularly pronounced in fibrous VC precipitates with higher amounts of manganese and iron than spherical/ellipsoidal VC precipitates. For the LCLV-RP sample, the majority of VC nanoprecipitates indicate nearly uniform iron and manganese distributions

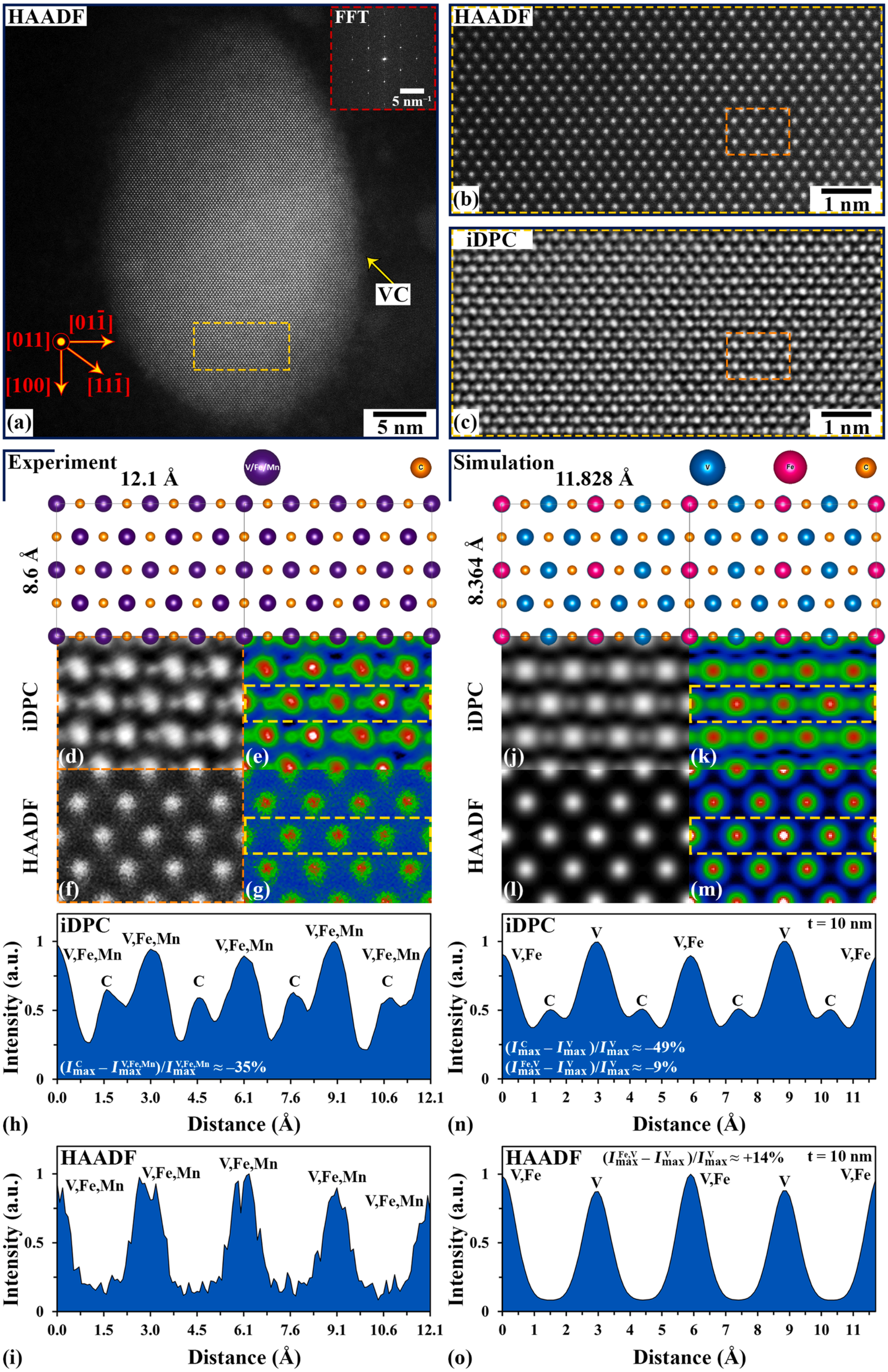

Fig. 2. Atomic-resolution microscopy of VC nanoprecipitates. **(a)** HAADF-STEM image of a grain-boundary precipitated VC along the [110] zone axis from the LCLV-IP CER. The inset indicates the fast Fourier transform (FFT) of the precipitate. **(b)** and **(c)** Atomic-resolution HAADF-STEM and iDPC-STEM images from the indicated region in **(a)**, respectively. **(d, e)** and **(f, g)** Experimental iDPC-STEM and HAADF-STEM images from the indicated regions in **(c)** and **(b)** in two different color maps (grayscale and polar—see Fig. S8), respectively. **(h)** and **(i)** iDPC-STEM and HAADF-STEM intensity profile analyses of the atomic columns along the central horizontal line within the indicated regions in **(e)** and **(g)**, respectively. **(j–o)** Corresponding simulated STEM images and associated intensity profile analyses of iron-doped vanadium carbide with a stoichiometry of $Fe_{0.125}V_{0.875}C$ and with a thickness of 10 nm along the [110] zone axis. An optimum defocus value of –2 nm was used for the simulations.

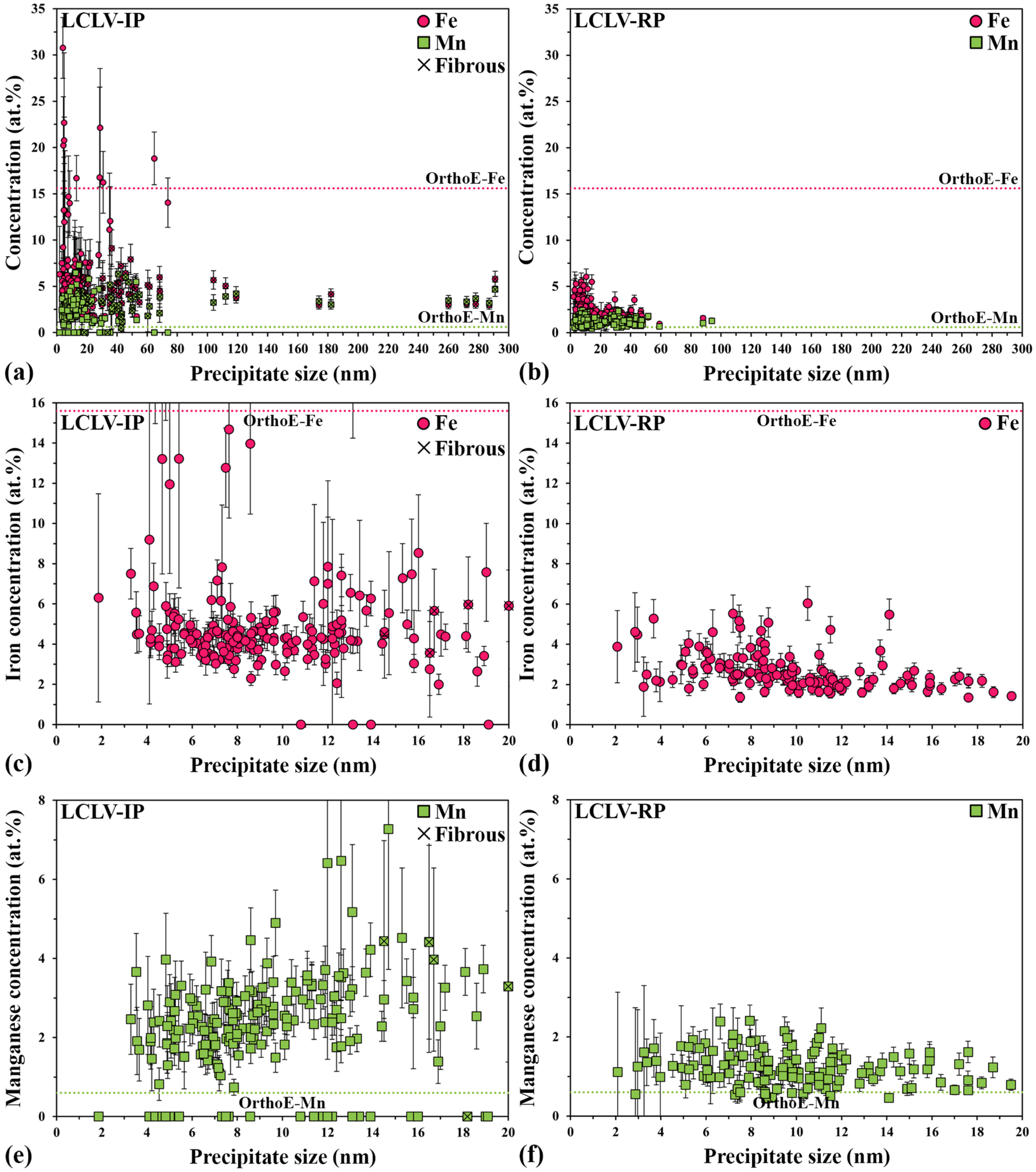

Fig. 3. Variations in the chemical composition of VC. (a) and **(b)** Results of STEM-EDS SI analyses showing iron and manganese concentrations (as site fractions) for a wide range of VC nanoprecipitate sizes observed in the LCLV-IP and LCLV-RP CERs, respectively. **(c–f)** Enlarged views of the data represented in **(a)** and **(b)**. Fibrous precipitates observed in the LCLV-IP sample are marked in **(a)**, **(c)**, and **(e)**. Precipitate size is defined as the largest measured dimension of individual nanoprecipitates. Orthoequilibrium concentration values of iron and manganese (as site fractions) in VC are indicated as dotted lines in the graphs. Error bars represent atomic (site) fraction errors reported by Velox software.

with concentrations well below those of the LCLV-IP sample (Fig. 5(o) and (p)). However, a few coarser VC precipitates contain higher iron and manganese contents than the finer precipitates, with compositional variations that suggest a core–shell-like elemental distribution (Fig. 5 (o)). It should be noted that the EDS spectrum profiles are all limited within the nanoprecipitates to prevent an overestimation of the iron and manganese atomic concentrations near precipitate/replica interfaces due to the exclusion of carbon in the quantification process.

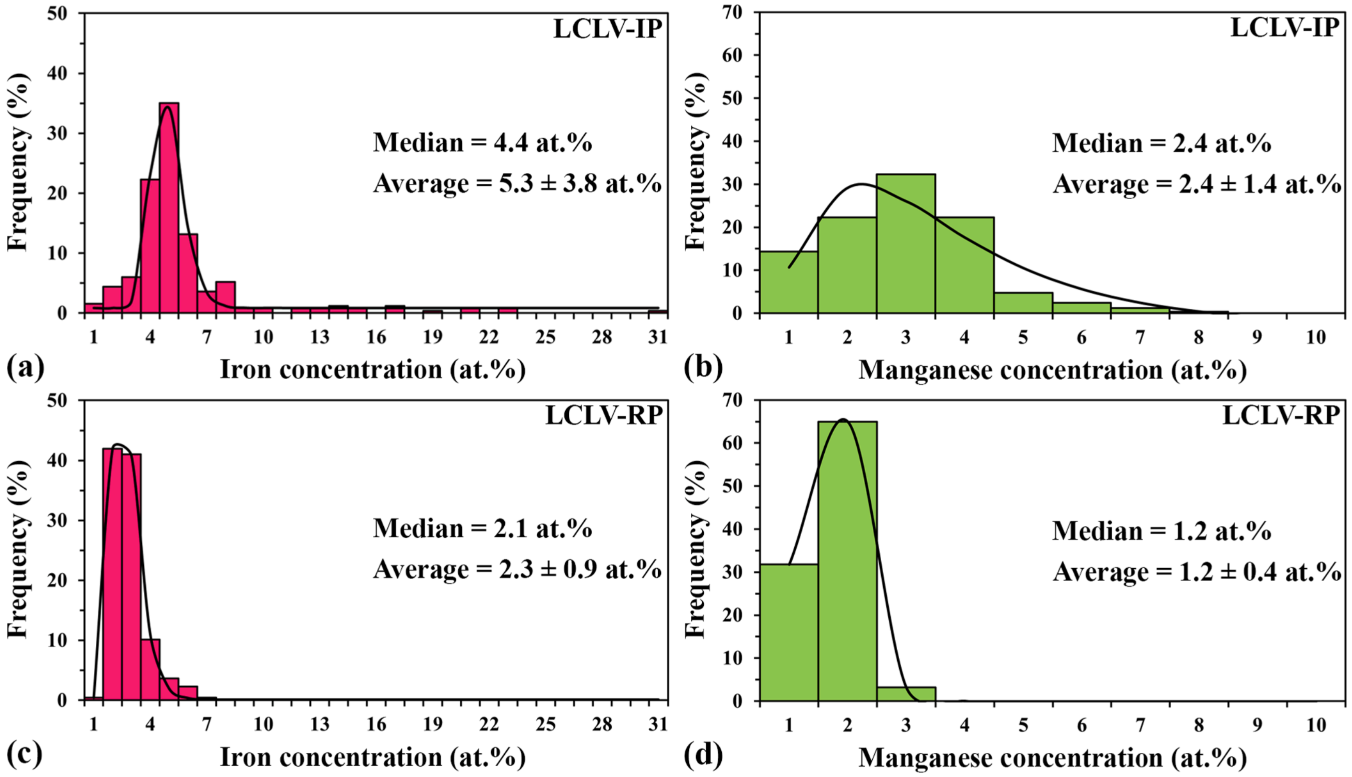

Fig. 4. Statistics for the chemical variability of VC nanoprecipitates. (a, b) and **(c, d)** Histograms of iron and manganese concentration distributions (as site fractions) for the LCLV-IP and LCLV-RP samples, respectively. Plus/minus error values indicate standard deviation.

4. Discussion

4.1. VC chemical complexity: interphase versus random precipitation mechanisms

Distinct variations in the chemical composition of VC nanoprecipitates are observed for the interphase and random precipitation conditions, where interphase precipitates contain higher amounts of iron and manganese, deviating from the orthoequilibrium concentration values (Figs. 3 and 4). Although the STEM-EDS SI technique effectively determines the concentration of iron and manganese within the precipitates, the carbon concentration level cannot be measured accurately, limiting the information on the compositional space of VC nanoprecipitates. To this end, a complementary SANS analysis was performed with the aim of mapping the *A*-factor as a function of iron, manganese, and carbon in nanoprecipitates. As illustrated in Fig. 6, ternary plots of the *A*-factor value can be obtained by systematic variations of iron and manganese site fractions (with a balanced vanadium site fraction) for fixed values of carbon site fraction using Eq. (1). Three different carbon site fractions, y, of 0.75, 0.875 (orthoequilibrium value at 650 °C), and 1 were considered, corresponding to M_4C_3, M_8C_7, and MC stoichiometries, respectively.

By increasing the carbon site fraction (reducing carbon vacancies) within the precipitates, the *A*-factor decreases for a given composition in the ternary plots (Fig. 6). Similarly, increasing the iron site fraction at constant values of manganese (along a line parallel to the V–Fe side of the triangle, e.g., the white dashed arrow in Fig. 6(a)) and carbon contents reduces the *A*-factor, which is also consistent with previous findings [27]. The opposite behavior is observed for an increasing manganese site fraction, where the calculated *A*-factor increases at constant values of iron and carbon site fractions (e.g., the white dotted arrow in Fig. 6(a)).

The mean experimental *A*-factor values are 0.92 ± 0.06 and 1.08 ± 0.05 for the LCLV-IP and LCLV-RP samples, respectively (see Fig. S11). By inserting these values in Eq. (1), various combinations of iron and manganese contents in VC nanoprecipitates can be calculated for the given carbon site fractions, which are plotted as black and purple lines in the ternary graphs (Fig. 6). Increasing the amount of carbon shifts the composition lines to lower iron and higher manganese concentrations. Moreover, a higher iron concentration is clearly associated with a higher manganese concentration within VC nanoprecipitates of both samples. Such variations are also evident from individual STEM-EDS SI measurements (Fig. 5), suggesting the tendency for co-incorporation of iron and manganese into the precipitates.

Comparing the STEM-EDS data with the SANS data indicates that the carbon site fraction of 0.75 shows a good agreement between the two techniques, in particular for the LCLV-RP sample. The SANS data further confirm that the orthoequilibrium composition is far from the estimated compositions. Since the VC composition can lie anywhere on the black and purple lines in Fig. 6, the iron and manganese contents from the STEM-EDS SI measurements are separately used to calculate the manganese and iron site fractions from the SANS data, respectively. Table 2 lists the corresponding values for the average chemical composition of VC under different conditions. The best agreement among the STEM and SANS data is achieved when the manganese is fixed by the STEM-EDS data. This gives an iron site fraction of 2.3% by the SANS measurements for VC nanoprecipitates of the LCLV-RP sample, whereas a value of 10.0% is derived for the iron site fraction within VC precipitates in the LCLV-IP sample, which is higher than the 5.3% obtained by the STEM measurements. Fixing the iron content in the calculations produces non-physical (negative) site fractions for the manganese and vanadium for the LCLV-IP sample, which is also perceived by looking at the SANS composition range with respect to the STEM average composition (Fig. 6 (a)).

A possible reason for the observed discrepancy in iron concentrations within VC precipitates between the two techniques lies in the inherent differences in data sampling and interpretation. As a bulk characterization method, the SANS technique provides statistically averaged

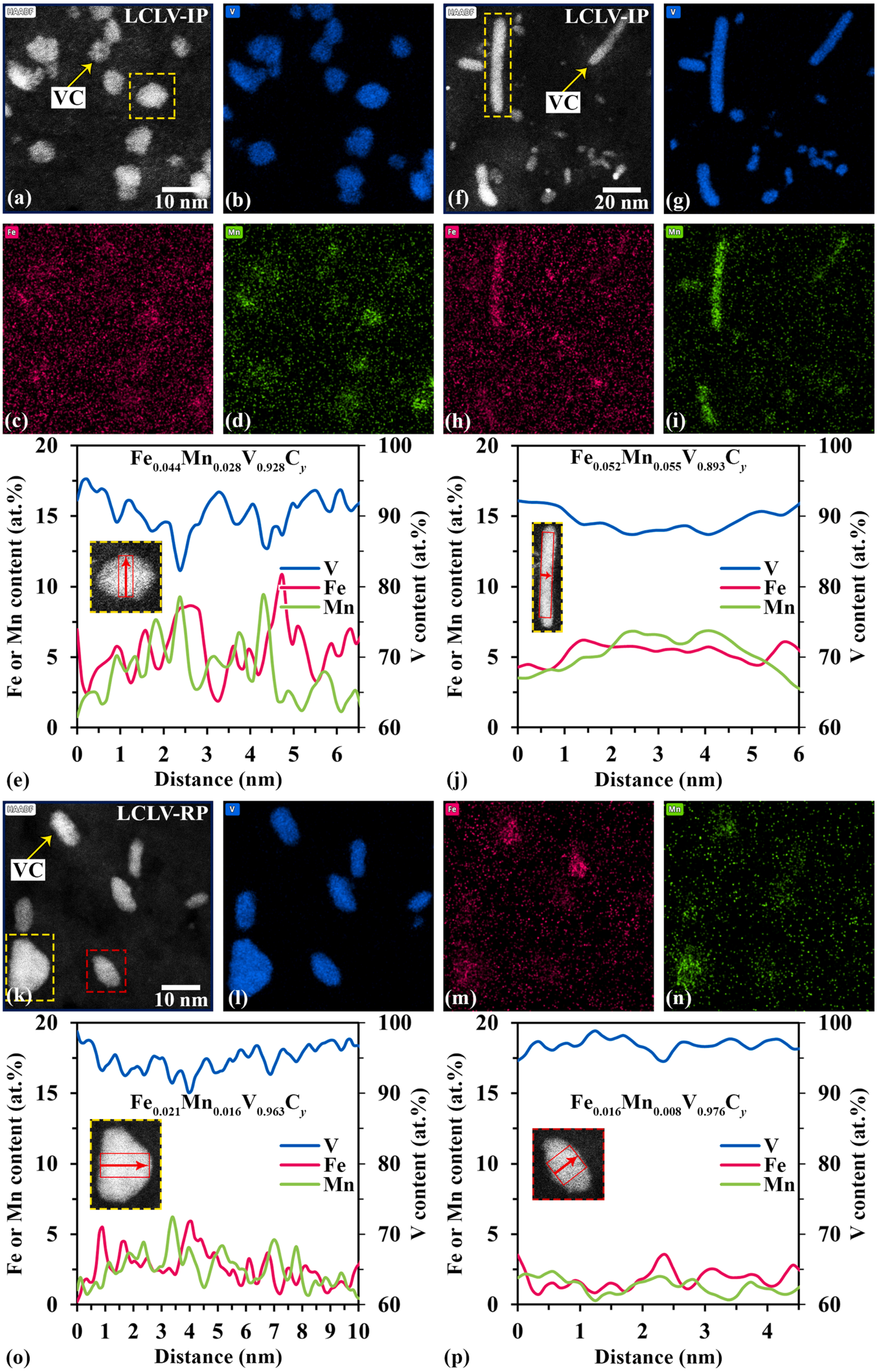

(caption on next page)

Fig. 5. Elemental maps of VC nanoprecipitates. (a–d) and **(f–i)** HAADF-STEM images associated with STEM-EDS SI elemental maps of spherical/ellipsoidal and fibrous VC in the LCLV-IP CER, respectively. **(e)** and **(j)** Corresponding STEM-EDS SI line profiles of iron, manganese, and vanadium atomic concentrations (as site fractions) for the precipitates marked by dashed rectangles in **(a)** and **(f)**, obtained by integrating the EDS signal perpendicular to the profile direction within the solid rectangles, as indicated by the red arrows in the insets, respectively. **(k–n)** HAADF-STEM image associated with STEM-EDS SI elemental maps of ellipsoidal/irregular VC in the LCLV-RP CER. **(o)** and **(p)** Corresponding STEM-EDS SI line profiles of iron, manganese, and vanadium atomic concentrations (as site fractions) for the precipitates marked by dashed rectangles in **(k)**, obtained by integrating the EDS signal perpendicular to the profile direction within the solid rectangles, as indicated by the red arrows in the insets. The average chemical compositions of the analyzed precipitates are also provided in the graphs. The elemental mass fraction maps are based on the relevant K_α X-ray peaks, and the contrast limits are normalized individually.

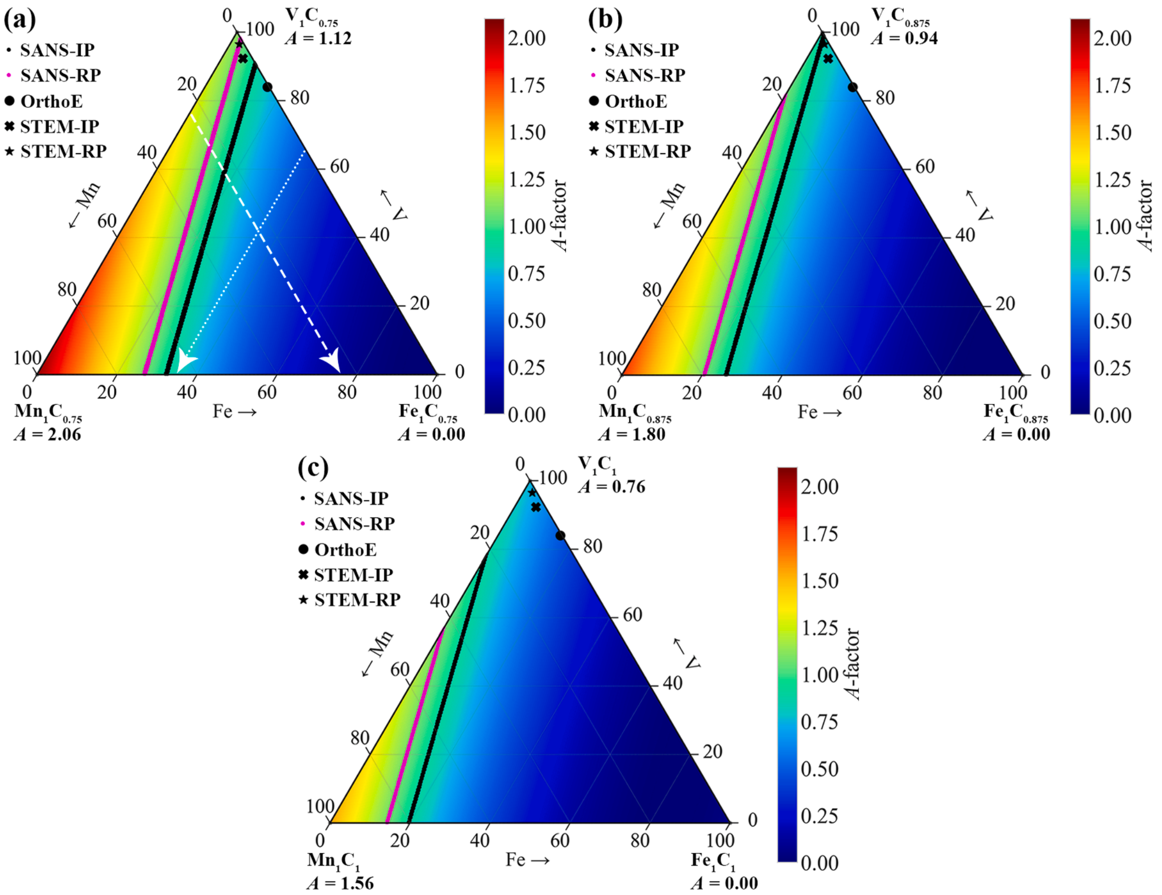

Fig. 6. Chemical composition space of VC analyzed by SANS. (a), (b), and **(c)** Ternary diagrams illustrating computed A-factor variations in the V–Fe–Mn chemical composition space for three different carbon site fractions of 0.75, 0.875, and 1, respectively. The chemical composition of VC nanoprecipitates lies anywhere on the black and purple lines for the LCLV-IP and LCLV-RP samples, respectively, according to mean experimental A-factor values measured by SANS. White dashed and dotted arrows in **(a)** are example manganese and iron isoconcentration lines, respectively.

Table 2

Summary of the average chemical composition of VC nanoprecipitates evaluated by STEM and SANS methods in this study for the LCLV-IP and LCLV-RP samples. The chemical composition of the VC precipitate corresponds to $Fe_xMn_zV_{1-x-z}C_y$, and the values x, y, and z are site fractions.

Sample (method)$_{\text{comment}}$	Fe (%)	Mn (%)	V (%)	C (%)
LCLV-IP (STEM)	5.3	2.4	92.3	—
LCLV-IP (SANS)$_{\text{Fe fixed by STEM}}$	5.3	—	—	75.0
LCLV-IP (SANS)$_{\text{Fe fixed by OrthoE}}$	15.6	18.8	65.6	75.0
LCLV-IP (SANS)$_{\text{Mn fixed by STEM}}$	10.0	2.4	87.6	75.0
LCLV-IP (SANS)$_{\text{Mn fixed by OrthoE}}$	9.4	0.6	90.0	75.0
LCLV-RP (STEM)	2.3	1.2	96.5	—
LCLV-RP (SANS)$_{\text{Fe fixed by STEM}}$	2.3	1.1	96.6	75.0
LCLV-RP (SANS)$_{\text{Fe fixed by OrthoE}}$	15.6	40.1	44.3	75.0
LCLV-RP (SANS)$_{\text{Mn fixed by STEM}}$	2.3	1.2	96.5	75.0
LCLV-RP (SANS)$_{\text{Mn fixed by OrthoE}}$	2.1	0.6	97.3	75.0
LCLV-IP/RP (OrthoE)$_{\text{Temperature at 650 °C}}$	15.6	0.6	83.8	87.2

information over the entire sampling volume, encompassing a distribution of precipitate morphologies (spherical, ellipsoidal, and fibrous) depending on their relative abundance. In the LCLV-IP sample, elongated fibrous VC precipitates (Fig. 1(c)) contain higher manganese concentrations than the more common spherical or ellipsoidal nanoprecipitates (Figs. 3 and 5). Among the scattering elements involved in the SANS experiments (i.e., Fe, Mn, V, and C), manganese provides the strongest contrast for the nuclear SANS [56], making the A-factor particularly sensitive to variations in the manganese content of the precipitates. The discrepancy can also be related to the accuracy of the chosen site fraction of carbon within the precipitates for the two samples, which directly affects the location of the composition lines in the ternary plots (Fig. 6). An increase in the carbon site fraction, y, shifts the composition line of VC toward the experimental STEM data point for the LCLV-IP sample, resulting in a comparable value of the iron site fraction at the same level of the manganese concentration (Fig. 6(a)).

The current STEM data, supported by room-temperature SANS measurements, indicate a significantly lower iron enrichment in interphase VC nanoprecipitates in comparison to the earlier high-temperature SANS results reported by Ioannidou and coworkers [27]. In that study, the iron site fraction was as high as 70% during the initial stages of the interphase VC precipitation, gradually decreasing to approximately 50% after 20 min of isothermal aging at 650 °C, and eventually reaching the orthoequilibrium value of around 16% after 600 min of aging. Here, the aging time corresponding to completion of the austenite-to-ferrite phase transformation is considered for the LCLV-IP sample [38,41]. This condition does not represent a purely early stage of interphase VC precipitation, but rather a mixed state in which earlier-formed ferrite grains coexist with continued precipitate growth. Consequently, nanoprecipitates spanning a range of sizes and thus different stages of VC evolution are analyzed by STEM-EDS SI. Despite this broad size distribution, comparably large variations in the iron site fraction are not observed (Fig. 3). A possible source of discrepancy may be related to the applied magnetic field during high-temperature SANS measurements and its influence on austenite-to-ferrite phase transformation kinetics together with VC evolution [27,40]. The assumption of magnetic behavior of iron incorporated in VC nanoprecipitates may also affect the compositions evaluated from high-temperature SANS data [27]. Although APT measurements in earlier studies indicate large variations in iron content, ranging from nearly zero at the precipitate core to above 80 at.% near the precipitate/matrix interface [27,41], these results can be affected by the local magnification effect during APT analysis. This effect creates an artifact, in which differences in field-evaporation potential between the precipitates and the iron matrix degrade spatial resolution in the vicinity of the precipitates [27,30,34]. On the other hand, concerns may also arise regarding possible dissolution of iron from the VC lattice during CER preparation, potentially leading to an underestimation of iron content. However, the methodology used here is less aggressive than conventional procedures [38] and yields results consistent with earlier CER studies [37] and with current room-temperature SANS measurements (Table 2). Additionally, manganese enrichment in VC nanoprecipitates has not been clearly reported in prior APT studies [15,27,41,57–59]. A plausible explanation is the similarity between the average manganese contents of the precipitate and the matrix, which can obscure enrichment in conventional manganese isoconcentration APT maps.

Current results suggest a much lower iron incorporation in interphase and random VC nanoprecipitates than even the orthoequilibrium concentration for the majority of precipitates (Fig. 3), challenging the hypothesis about the role of iron in reducing the precipitate–matrix lattice misfit strain. By considering a variation of manganese in VC nanoprecipitates, which to the best of the authors' knowledge has not been reported previously, the observed chemical complexity may be attributed to the (co-)segregation of manganese and iron at VC nucleation sites in the LCLV-IP and LCLV-RP samples, as discussed in more detail in Section 4.2. In particular, the segregation of manganese at the α/γ interface in the case of interphase precipitation and at matrix dislocations in the case of random precipitation is not adequately accounted for in the calculation of the orthoequilibrium composition. Consequently, deviations between the actual and orthoequilibrium compositions of the VC precipitates are to be expected.

4.2. VC nanoprecipitates with inherited manganese heterogeneity

Generally, α/γ interfaces and dislocations are the main nucleation sites for the interphase and random precipitation mechanisms, respectively [17,60]. Apparent differences in the nature of these nucleation sites coupled with the governing kinetic and thermodynamic conditions at the precipitate–matrix interface during precipitation dictate the chemical evolution of the nanoprecipitates. The majority of interphase VC nanoprecipitates in the LCLV-IP sample contain higher amounts of manganese and iron compared to random VC nanoprecipitates in the LCLV-RP sample (Figs. 3 and 4). The core–shell-like distribution of manganese is not only observed in spherical/elliptical precipitates, but is even more pronounced in fibrous VC nanoprecipitates (Fig. 5(j)). Fig. 7 provides high-resolution structural imaging and chemical analysis data of an elongated fibrous VC precipitate, similar to those perpendicular to the interface in Fig. 1(c). The HAADF-STEM intensity variations along the length of the precipitate predominantly correlate to the channeling effect of imaging electrons due to changes in the relative orientation of the precipitate during CER preparation (Fig. 7(a)).

Nevertheless, this fibrous VC indicates a growth direction of $\langle 100 \rangle$ (Fig. 7(b)), corresponding to the original Baker–Nutting orientation relationship of $\{100\}_F \,||\, \{100\}_{VC}$, $\langle 100 \rangle_F \,||\, \langle 110 \rangle_{VC}$ [61]. The STEM-EDS SI analysis of this precipitate shows intriguing features; not only is a core–shell-like distribution of manganese observed, but manganese and iron also vary along the length of the precipitate (Fig. 7(c–h) and Fig. S12). The peaks of iron and manganese concentrations (as site fractions) simultaneously reach values as high as 10 at.% in the core of the precipitate (Fig. 7(h)), suggesting co-incorporation of these elements during VC precipitation.

Recent experimental and theoretical studies indicate that interphase precipitation occurs at mobile α/γ interfaces with pronounced solute concentration spikes [16,47,62,63]. However, direct evidence of such dynamically formed concentration spikes being retained within the nanoscale precipitates has not yet been captured. It has been reported that fibrous VC precipitates are formed during interphase precipitation when the α/γ interface velocity is reduced, leading to the growth of VC precipitates normal to the interface [9,50–52]. The formation of fibrous precipitates is promoted in alloys with a higher manganese content and is further enhanced by the addition of molybdenum [9,50–52]. It is proposed that the segregation of manganese (and more strongly that of molybdenum) at the α/γ interface and the associated SDE reduce the interface velocity and, consequently, trigger the formation of fibrous VC precipitates.

To evaluate this hypothesis, SDE modeling was performed for the LCLV-IP sample using Eqs. (2–5), and the results are illustrated in Fig. 8. The α/γ interface velocity was determined under the assumption of a planar interface using the relation $v(t) = r_\gamma df(t)/dt$, where r_γ is the radius of the prior austenite grain (set as 30 μm) and $f(t)$, derived from the dilatometry data, represents the fraction of transformed austenite. Fig. 8(a) shows the fraction of transformed austenite along with the α/γ interface velocity during isothermal holding at 650 °C. After reaching a peak value of approximately 150 nm s^{-1} at about 1 min of isothermal holding (about 40% of transformed austenite), the interface velocity gradually decreases during the austenite-to-ferrite phase transformation, reaching about 0.2 nm s^{-1} after 20 min of isothermal holding.

The total Gibbs free energy dissipation as a function of the α/γ interface velocity is shown in Fig. 8(b). This also includes the contribution of interface friction, expressed as $\Delta G_{IF} = v(t)/M$, where M is the intrinsic mobility of the α/γ interface. For the reconstructive γ → α phase transformation with incoherent interfaces, the interface mobility is a thermally activated quantity that follows the Arrhenius relation $M = M_0 \exp(-Q/RT)$, where M_0 denotes the pre-exponential factor, Q is the activation energy (135–150 kJ mol^{-1}), R is the gas constant (8.31 J mol^{-1} K^{-1}), and T is the absolute temperature. Reported values of M_0 vary by several orders of magnitude [64], which explains the wide scatter in measured α/γ interface mobility. Here, the M_0 value listed in Table S3 was used to evaluate the interface mobility.

Immediately after ferrite nucleation, interface friction is the rate-controlling process, as the small amount of carbon rejected from the growing ferrite phase can readily diffuse into the austenite bulk. At this stage, the interface velocity lies in the range of 80–150 nm s^{-1}, with interface friction dominating the total energy dissipation (Fig. 8(b)). Once the α/γ interface velocity falls below the value corresponding to the minimum in the total dissipated energy (about 60 nm s^{-1}), the SDE (particularly from manganese) becomes significant, causing a rapid reduction in the interface velocity. Simultaneously, manganese segregation at the α/γ interface increases, as illustrated in Fig. 8(c). The integrated manganese site fraction at the α/γ interface increases from nearly 2% to 7% as the interface velocity decreases from about 100 to

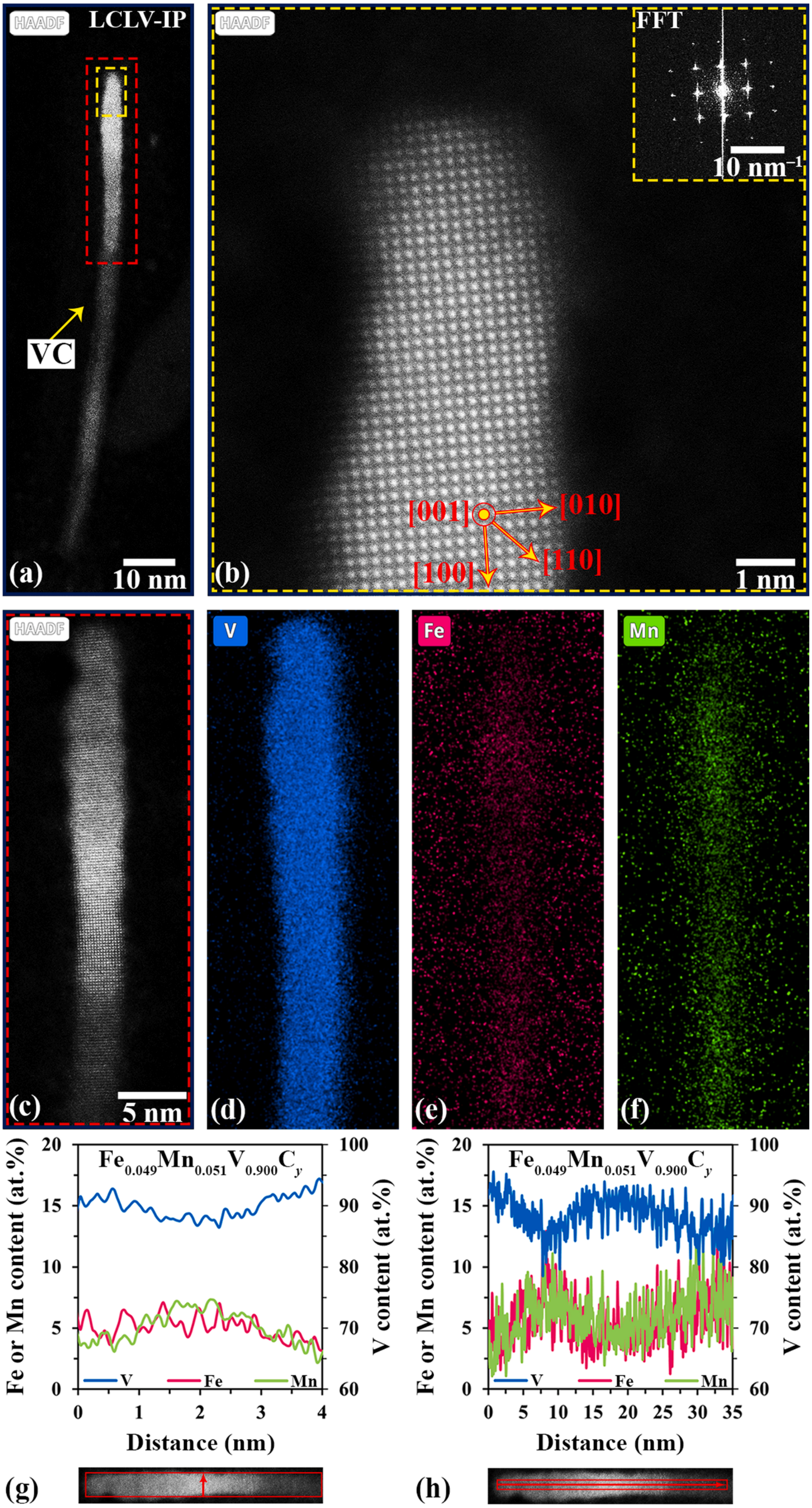

(caption on next page)

Fig. 7. Core–shell-like structure of fibrous VC nanoprecipitates. (a) HAADF-STEM image of an elongated fibrous VC from the LCLV-IP CER. **(b)** Atomic-resolution HAADF-STEM image from the region indicated by the yellow dashed rectangle in **(a)** along the [001] zone axis of the precipitate. The inset shows the fast Fourier transform (FFT) of the precipitate. **(c–f)** HAADF-STEM image associated with high-resolution STEM-EDS SI elemental maps of the precipitate from the region indicated by the red dashed rectangle in **(a). (g)** and **(h)** Corresponding STEM-EDS SI line profiles of iron, manganese, and vanadium atomic concentrations (as site fractions), measured across and along the precipitate length with the EDS signal integrated perpendicular to the profile direction within the solid rectangles, as indicated by the red arrows below the graphs. The average chemical composition of the precipitate is also provided in the graphs. The elemental mass fraction maps are based on the relevant K_α X-ray peaks, and the contrast limits are normalized individually.

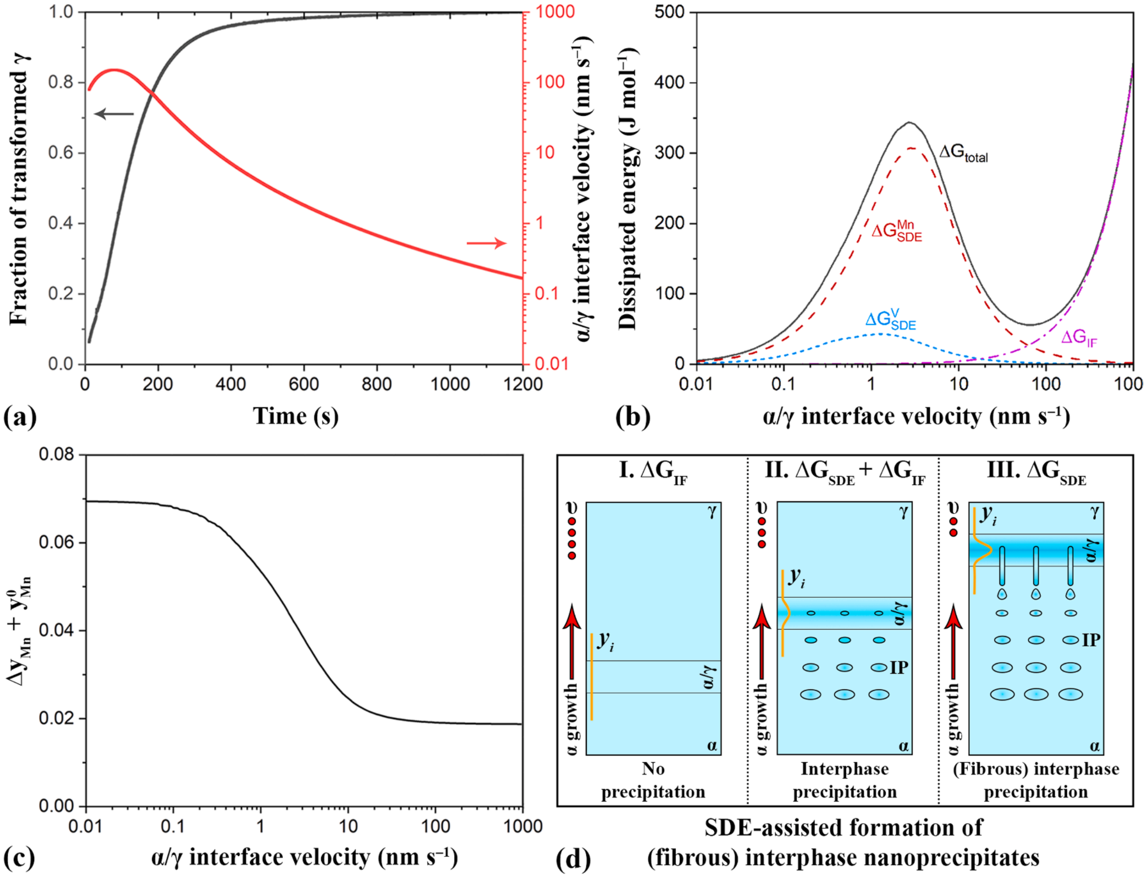

Fig. 8. Solute-drag effect (SDE) and its correlation to the formation of chemical heterogeneity within (fibrous) interphase VC nanoprecipitates. (a) Ferrite/austenite (α/γ) interface velocity along with the transformed γ fraction as a function of time during the isothermal γ → α phase transformation at 650 °C for 20 min in the LCLV-IP sample. **(b)** Individual Gibbs free energy dissipators (SDEs and interface friction (IF)) and their combination as a function of the α/γ interface velocity. **(c)** Variations in the integrated manganese site fraction within the α/γ interface as a function of the interface velocity. **(d)** Schematic illustrations of the formation of chemically heterogeneous (fibrous) interphase VC nanoprecipitates at different α/γ interface velocities (υ), highlighting the dominant Gibbs free energy dissipators.

0.1 nm s^{-1}. This is in good agreement with the experimental STEM-EDS SI measurements of the inherited manganese content in interphase VC nanoprecipitates, assuming their formation at the α/γ interface under negligible partitioning local equilibrium (NPLE) conditions [57]. The modeling data support local variations in the manganese concentration within fibrous VC nanoprecipitates during their dynamic formation (Fig. 5(e), 5(j), and 7). Additionally, SANS measurements on the same LCLV alloy detect the first signal of interphase VC formation after 2.5–3 min of isothermal holding at 650 °C [41]. This stage of the phase transformation corresponds to 65–75% austenite decomposition and an α/γ interface velocity of 80–100 nm s^{-1}, where both solute drag and interface friction act as the dominant Gibbs free energy dissipators (Fig. 8(a) and (b)). This implies the absence of VC precipitation at relatively high interface velocities and further supports the facilitation of interphase VC precipitation by the SDE at lower interface velocities. All these results provide the first direct validation of the hypothesis that the manganese SDE plays a decisive role in the formation of (fibrous) interphase VC precipitates, as schematically illustrated in Fig. 8(d).

Furthermore, the observed direct correlation between iron and manganese concentrations in VC nanoprecipitates likely stems from the co-segregation tendency of these elements during VC precipitation (Figs. 4 and 6). As no correlation is found between the precipitate size and the corresponding iron and manganese concentrations (Fig. 3), the elastic strain energy from precipitate–matrix lattice misfit and the Gibbs–Thomson effect associated with precipitate–matrix interfacial energy are not dominant factors in the chemical evolution of VC nanoprecipitates. Indeed, the observed chemical variations can be directly linked to the nanoscale non-equilibrium local compositions at the active nucleation sites and in the surrounding matrix where the precipitates form. However, the present experimental data do not resolve whether iron and manganese enrichment in VC nanoprecipitates occurs during or immediately after nucleation events. As discussed for the interphase precipitation mechanism (Figs. 7 and 8), a similar argument can be applied for the random precipitation mechanism in the LCLV-RP sample, where dislocations are considered as active precipitation nucleation sites. Strong experimental evidence supports manganese segregation at dislocation cores [65–67]. Local manganese enrichment in the matrix has a negligible effect on the chemical driving force for VC precipitation (see Fig. S13). Subsequent nucleation and growth of VC nanoprecipitates on such dislocations lead to the formation of manganese-rich–core precipitates with co-incorporated iron, although with lower concentrations than those of interphase precipitates (Fig. 4–6).

As mentioned in Section 3.1, random VC precipitates may also form in certain ferrite grains of the LCLV-IP sample where the interphase precipitation reaction cannot proceed (Figs. 1(c) and 8(d)). The STEM-EDS SI data points showing lower levels of iron and manganese within VC in the LCLV-IP sample may correspond to such random VC precipitates (Fig. 3). Nevertheless, the average iron and manganese concentrations in the nanoprecipitates are respectively lower and higher than their orthoequilibrium values for both samples (Table 2), which could indicate that manganese enrichment alters the iron solubility in VC precipitates due to segregation effects (Fig. S13). These findings demonstrate that solute transport mechanisms, operating either during the austenite-to-ferrite phase transformation or subsequent matrix aging, govern the chemical complexity of VC precipitates. This mechanistic understanding provides a foundation for tuning the nanoscale chemistry of these carbides and thereby tailoring precipitation strengthening in microalloyed steels, an aspect that will be further explored in future studies.

5. Conclusions

The chemical composition of vanadium carbide (VC) nanoprecipitates has been systematically investigated using atomic-resolution scanning transmission electron microscopy (STEM) techniques, complemented by an analysis of room-temperature small-angle neutron scattering (SANS) results and solute-drag effect (SDE) modeling. A low-carbon low-vanadium (LCLV) model steel featuring predominantly ferritic and bainitic microstructures has been employed to compare the chemical complexity of VC precipitates formed through interphase precipitation (IP) and random precipitation (RP) mechanisms during aging at 650 °C for 20 min. The following conclusions are drawn:

(1) Carbon sublattice atoms are simultaneously imaged alongside vanadium–iron–manganese sublattice atoms in VC nanoprecipitates using integrated differential phase-contrast STEM (iDPC-STEM). However, atomic-resolution high-angle annular dark-field STEM (HAADF-STEM) and iDPC-STEM simulations reveal that direct imaging of iron within VC nanoprecipitates is only feasible if the iron forms an ordered sublattice in the VC crystal structure—an arrangement not supported by experimental observations. Nevertheless, atomic-scale STEM energy-dispersive X-ray spectroscopy spectrum imaging (STEM-EDS SI) effectively maps the distribution of both iron and manganese within the precipitates.

(2) Interphase VC nanoprecipitates exhibit higher concentrations of iron and manganese than random VC nanoprecipitates. The corresponding chemical formulas are $Fe_{0.053}Mn_{0.024}V_{0.923}C_y$ for the LCLV-IP sample and $Fe_{0.023}Mn_{0.012}V_{0.965}C_y$ for the LCLV-RP sample, with a mean carbon site fraction $y = 0.75$ estimated from SANS measurements.

(3) No correlation is found between VC nanoprecipitate size and corresponding iron or manganese content. This suggests that the elastic strain energy from precipitate–matrix lattice misfit and the Gibbs–Thomson effect related to precipitate–matrix interfacial energy do not significantly influence the chemical evolution of VC.

(4) The formation of (fibrous) interphase VC precipitates via the SDE is experimentally validated by high-resolution STEM-EDS SI and further supported by numerical modeling. Dynamic manganese segregation at moving ferrite/austenite interfaces promotes the formation of manganese-rich–core (fibrous) interphase precipitates with co-incorporated iron. A similar, albeit less pronounced, mechanism is proposed for random VC precipitates, involving manganese segregation at dislocations.

(5) The co-segregation tendency of iron and manganese in VC nanoprecipitates is revealed by atomic-scale STEM-EDS SI and supported by SANS results. Manganese enrichment is proposed to change the iron solubility in VC due to segregation effects (mentioned in (4)), leading to lower iron and higher manganese concentrations in the precipitates compared to the orthoequilibrium values for both samples.

Data availability

All raw and processed data required to reproduce the findings of this study are available from the corresponding authors upon reasonable request.

CRediT authorship contribution statement

Amir Sabet Ghorabaei: Writing – review & editing, Writing – original draft, Visualization, Validation, Project administration, Methodology, Investigation, Formal analysis, Data curation, Conceptualization. **Maria Giuseppina Mecozzi:** Writing – review & editing, Writing – original draft, Visualization, Validation, Methodology, Investigation, Formal analysis, Data curation. **Zamran Zahoor Khan:** Writing – review & editing, Writing – original draft, Visualization, Validation, Methodology, Investigation, Formal analysis, Data curation. **Majid Ahmadi:** Writing – review & editing, Methodology. **Steven R. Parnell:** Writing – review & editing, Validation, Supervision, Methodology. **Sven Erik Offerman:** Writing – review & editing, Validation, Supervision, Resources, Project administration, Methodology, Funding acquisition, Data curation. **Niels H. van Dijk:** Writing – review & editing, Validation, Supervision, Resources, Project administration, Methodology, Funding acquisition, Data curation. **Bart J. Kooi:** Writing – review & editing, Validation, Supervision, Resources, Project administration, Methodology, Funding acquisition, Data curation, Conceptualization.

Declaration of competing interest

The authors declare that they have no known competing financial interests or personal relationships that could have appeared to influence the work reported in this paper.

Acknowledgments

This research was carried out under project number 19470-NWO/N21014-M2i in the framework of the Partnership Program of the Materials innovation institute M2i (www.m2i.nl) and the Technology Foundation TTW (www.stw.nl), which is part of the Netherlands Organization for Scientific Research (www.nwo.nl). Tata Steel (IJmuiden, The Netherlands) is acknowledged for providing the material for this study. A.S.G., M.A., and B.J.K. are grateful for the financial support from the Zernike Institute for Advanced Materials (ZIAM) and the Groningen Cognitive Systems and Materials Center (CogniGron) to the ZIAM electron microscopy facilities at the University of Groningen. The authors acknowledge the use of the Zoom instrument at ISIS Pulsed Neutron and Muon Source (Harwell Oxford, United Kingdom). The SANS data can be found at https://doi.org/10.5286/ISIS.E.RB2310339-1. The authors would like to thank Dr. Arjan Rijkenberg (Tata Steel) for his contributions to alloy design and process development, and Dr. Winfried Kranendonk (Tata Steel) for his contributions to SDE modeling. A.S.G. sincerely thanks Dr. Gert ten Brink (University of Groningen) and Dr. Marc Stuart (University of Groningen) for their technical support. A.S.G. dedicates this research to the memory of his mother, Mahin Sadat Mirian.

Supplementary materials

Supplementary material associated with this article can be found, in the online version, at doi:10.1016/j.actamat.2026.122061.

References

[1] Y. Funakawa, T. Shiozaki, K. Tomita, T. Yamamoto, E. Maeda, Development of high strength hot-rolled sheet steel consisting of ferrite and nanometer-sized carbides, ISIJ Int 44 (2004) 1945–1951.
[2] Y.-J. Zhang, E. Chandiran, H.-K. Dong, N. Kamikawa, G. Miyamoto, T. Furuhara, Current understanding of microstructure and properties of micro-alloyed low carbon steels strengthened by interphase precipitation of nano-sized alloy carbides: a review, JOM 73 (2021) 3214–3227.
[3] A.D. Batte, R.W.K. Honeycombe, Strengthening of ferrite by vanadium carbide precipitation, Met. Sci. 7 (1973) 160–168.
[4] T.N. Baker, Processes, microstructure and properties of vanadium microalloyed steels, Mater. Sci. Technol. 25 (2009) 1083–1107.
[5] G.L. Dunlop, R.W.K. Honeycombe, Ageing characteristics of VC, TiC, and (V, Ti)C dispersions in ferrite, Met. Sci. 12 (1978) 367–371.
[6] T.N. Baker, Titanium microalloyed steels, Ironmak. Steelmak. 46 (2019) 1–55.
[7] R. Okamoto, A. Borgenstam, J. Ågren, Interphase precipitation in niobium-microalloyed steels, Acta Mater 58 (2010) 4783–4790.
[8] P. Gong, E.J. Palmiere, W.M. Rainforth, Dissolution and precipitation behavior in steels microalloyed with niobium during thermomechanical processing, Acta Mater 97 (2015) 392–403.
[9] A. Barbacki, R.W.K. Honeycombe, Transitions in carbide morphology in molybdenum and vanadium steels, Metallogr 9 (1976) 277–291.
[10] S. Yamasaki, H.K.D.H. Bhadeshia, Modelling and characterization of Mo_2C precipitation and cementite dissolution during tempering of Fe–C–Mo martensitic steel, Mater. Sci. Technol. 19 (2003) 723–731.
[11] S. Mukherjee, I. Timokhina, C. Zhu, S.P. Ringer, P.D. Hodgson, Clustering and precipitation processes in a ferritic titanium-molybdenum microalloyed steel, J. Alloys Compd. 690 (2017) 621–632.
[12] P. Gong, X.G. Liu, A. Rijkenberg, W.M. Rainforth, The effect of molybdenum on interphase precipitation and microstructures in microalloyed steels containing titanium and vanadium, Acta Mater 161 (2018) 374–387.
[13] Z. Wang, H. Chen, Z. Yang, F. Jiang, Decelerated coarsening of (Ti, Mo)C particles with a core–shell structure in austenite of a Ti-Mo-bearing steel, Metall. Mater. Trans. A 49 (2018) 1455–1459.
[14] L. Jiang, R.K.W. Marceau, T. Dorin, K. Wood, P.D. Hodgson, N. Stanford, The effect of molybdenum on interphase precipitation at 700 °C in a strip-cast low-carbon niobium steel, Mater. Charact. 166 (2020) 110444.
[15] Y. Zhang, G. Miyamoto, T. Furuhara, Enhanced hardening by multiple microalloying in low carbon ferritic steels with interphase precipitation, Scr. Mater. 212 (2022) 114558.
[16] I. Bikmukhametov, H. Beladi, J. Wang, V. Tari, A.D. Rollett, P.D. Hodgson, I. Timokhina, Interface characteristics and precipitation during the austenite-to-ferrite transformation of a Ti-Mo microalloyed steel, J. Alloys. Compd. 893 (2022) 162224.
[17] R.W.K. Honeycombe, R.F. Mehl, Transformation from austenite in alloy steels, Metall. Trans. A 7 (1976) 915–936.
[18] R.A. Ricks, P.R. Howell, The formation of discrete precipitate dispersions on mobile interphase boundaries in iron-base alloys, Acta Metall 31 (1983) 853–861.
[19] H.-W. Yen, P.-Y. Chen, C.-Y. Huang, J.-R. Yang, Interphase precipitation of nanometer-sized carbides in a titanium–molybdenum-bearing low-carbon steel, Acta Mater 59 (2011) 6264–6274.
[20] Y.-J. Zhang, G. Miyamoto, K. Shinbo, T. Furuhara, T. Ohmura, T. Suzuki, K. Tsuzaki, Effects of transformation temperature on VC interphase precipitation and resultant hardness in low-carbon steels, Acta Mater 84 (2015) 375–384.
[21] S. Yamasaki, H.K.D.H. Bhadeshia, Modelling and characterization of V_4C_3 precipitation and cementite dissolution during tempering of Fe–C–V martensitic steel, Mater. Sci. Technol. 19 (2003) 1335–1343.
[22] C.E.I.C. Öhlund, J. Weidow, M. Thuvander, S.E. Offerman, Effect of Ti on evolution of microstructure and hardness of martensitic Fe–C–Mn steel during tempering, ISIJ Int 54 (2014) 2890–2899.
[23] X. Zhang, C. Ioannidou, G.H. ten Brink, A. Navarro-López, J. Wormann, J. Campaniello, R.M. Dalgliesh, A.A. van Well, S.E. Offerman, W. Kranendonk, B. J. Kooi, Microstructure, precipitate and property evolution in cold-rolled Ti-V high strength low alloy steel, Mater. Des. 192 (2020) 108720.
[24] E. Claesson, H. Magnusson, J. Kohlbrecher, M. Thuvander, P. Hedström, Evolution of iron carbides during tempering of low-alloy tool steel studied with polarized small angle neutron scattering, electron microscopy and atom probe, Mater. Charact. 194 (2022) 112464.
[25] H. Liu, J. Zhu, Y. Liu, Z. Lai, First-principles study on the mechanical properties of vanadium carbides VC and V_4C_3, Mater. Lett. 62 (2008) 3084–3086.
[26] X. Chong, Y. Jiang, R. Zhou, J. Feng, Electronic structures mechanical and thermal properties of V-C binary compounds, RSC Adv 4 (2014) 44959–44971.
[27] C. Ioannidou, A. Navarro-López, A. Rijkenberg, R.M. Dalgliesh, S. Koelling, C. Pappas, J. Sietsma, A.A. van Well, S.Erik Offerman, Evolution of the precipitate composition during annealing of vanadium micro-alloyed steels by in-situ SANS, Acta Mater 201 (2020) 217–230.
[28] F. Danoix, E. Bémont, P. Maugis, D. Blavette, Atom probe tomography I. Early stages of precipitation of NbC and NbN in ferritic steels, Adv. Eng. Mater. 8 (2006) 1202–1205.
[29] S. Mukherjee, I.B. Timokhina, C. Zhu, S.P. Ringer, P.D. Hodgson, Three-dimensional atom probe microscopy study of interphase precipitation and nanoclusters in thermomechanically treated titanium–molybdenum steels, Acta Mater 61 (2013) 2521–2530.
[30] S. Dhara, R.K.W. Marceau, K. Wood, T. Dorin, I.B. Timokhina, P.D. Hodgson, Precipitation and clustering in a Ti-Mo steel investigated using atom probe tomography and small-angle neutron scattering, Mater. Sci. Eng. A 718 (2018) 74–86.
[31] J. Wang, M. Weyland, I. Bikmukhametov, M.K. Miller, P.D. Hodgson, I. Timokhina, Transformation from cluster to nano-precipitate in microalloyed ferritic steel, Scr. Mater. 160 (2019) 53–57.
[32] Y. Zhang, G. Miyamoto, T. Furuhara, Atom probe compositional analysis of interphase precipitated nano-sized alloy carbide in multiple microalloyed low-carbon steels, Microsc. Microanal. 25 (2019) 447–453.
[33] P.-Y. Liu, B. Zhang, R. Niu, S.-L. Lu, C. Huang, M. Wang, F. Tian, Y. Mao, T. Li, P. A. Burr, H. Lu, A. Guo, H.-W. Yen, J.M. Cairney, H. Chen, Y.-S. Chen, Engineering metal-carbide hydrogen traps in steels, Nat. Commun. 15 (2024) 724.
[34] E.A. Marquis, J.M. Hyde, Applications of atom-probe tomography to the characterization of solute behaviors, Mater. Sci. Eng. R Rep. 69 (2010) 37–62.
[35] B. Gault, F. Danoix, K. Hoummada, D. Mangelinck, H. Leitner, Impact of directional walk on atom probe microanalysis, Ultramicroscopy 113 (2012) 182–191.
[36] N. Singh, G. Casillas, D. Wexler, C. Killmore, E. Pereloma, Application of advanced experimental techniques to elucidate the strengthening mechanisms operating in microalloyed ferritic steels with interphase precipitation, Acta Mater 201 (2020) 386–402.
[37] S.P. Duckworth, Z.X. Guo, T.N. Baker, A microanalytical study of the apparent iron content of vanadium carbide precipitates in HSLA Steel, Mater. Charact. 25 (1990) 17–36.
[38] A.S. Ghorabaei, B.J. Kooi, Optimized carbon extraction replicas for transmission electron microscopy of nanoprecipitates in microalloyed low-carbon steels, J. Mater. Res. Technol. 30 (2024) 6418–6429.
[39] Z.Z. Khan, S.R. Parnell, S.E. Offerman, D.A. Venero, A.S. Ghorabaei, B.J. Kooi, N. van Dijk, Interphase and random nanoscale carbide precipitation in vanadium micro-alloyed steels studied using SANS, J. Mater. Sci. 60 (2025) 7002–7019.
[40] C. Ioannidou, A. Navarro-López, R.M. Dalgliesh, A. Rijkenberg, X. Zhang, B. Kooi, N. Geerlofs, C. Pappas, J. Sietsma, A.A. van Well, S.E. Offerman, Phase-transformation and precipitation kinetics in vanadium micro-alloyed steels by in-situ, simultaneous neutron diffraction and SANS, Acta Mater 220 (2021) 117317.
[41] C. Ioannidou, Z. Arechabaleta, A. Navarro-López, A. Rijkenberg, R.M. Dalgliesh, S. Kölling, V. Bliznuk, C. Pappas, J. Sietsma, A.A. van Well, S.E. Offerman, Interaction of precipitation with austenite-to-ferrite phase transformation in vanadium micro-alloyed steels, Acta Mater 181 (2019) 10–24.
[42] I. Lazić, E.G.T. Bosch, S. Lazar, Phase contrast STEM for thin samples: integrated differential phase contrast, Ultramicroscopy 160 (2016) 265–280.
[43] S. de Graaf, J. Momand, C. Mitterbauer, S. Lazar, B.J. Kooi, Resolving hydrogen atoms at metal-metal hydride interfaces, Sci. Adv. 6 (2020) eaay4312.
[44] J. Barthel, Dr. Probe: a software for high-resolution STEM image simulation, Ultramicroscopy 193 (2018) 1–11.
[45] K. Momma, F. Izumi, VESTA 3 for three-dimensional visualization of crystal, volumetric and morphology data, J. Appl. Crystallogr. 44 (2011) 1272–1276.
[46] D.W. Bloom, L. Finegold, A. Tveten, R.G. Lye, Magnetic susceptibility of vanadium carbide, Philos. Mag. 24 (1971) 603–612.
[47] G. Miyamoto, K. Yokoyama, T. Furuhara, Quantitative analysis of Mo solute drag effect on ferrite and bainite transformations in Fe-0.4C-0.5Mo alloy, Acta Mater 177 (2019) 187–197.
[48] M. Hillert, B. Sundman, A treatment of the solute drag on moving grain boundaries and phase interfaces in binary alloys, Acta Metall 24 (1976) 731–743.
[49] B. Sundman, J. Ågren, A regular solution model for phases with several components and sublattices, suitable for computer applications, J. Phys. Chem. Solids 42 (1981) 297–301.
[50] F.A. Khalid, D.V. Edmonds, Interphase precipitation in microalloyed engineering steels and model alloy, Mater. Sci. Technol. 9 (1993) 384–396.
[51] M.-Y. Chen, H.-W. Yen, J.-R. Yang, The transition from interphase-precipitated carbides to fibrous carbides in a vanadium-containing medium-carbon steel, Scr. Mater. 68 (2013) 829–832.
[52] S. Mukherjee, I. Timokhina, J. Wang, A. Chakraborty, S. Pramanik, S. Kundu, P. D. Hodgson, Interphase and fibrous precipitation in a thermomechanically processed V–Nb–Mo microalloyed steel, Mater. Sci. Technol. 39 (2023) 1010–1020.
[53] G. Miyamoto, R. Hori, B. Poorganji, T. Furuhara, Crystallographic analysis of proeutectoid ferrite/austenite interface and interphase precipitation of vanadium carbide in medium-carbon steel, Metall. Mater. Trans. A 44 (2013) 3436–3443.
[54] Y.-J. Zhang, G. Miyamoto, K. Shinbo, T. Furuhara, Effects of α/γ orientation relationship on VC interphase precipitation in low-carbon steels, Scr. Mater. 69 (2013) 17–20.
[55] J.-O. Andersson, T. Helander, L. Höglund, P. Shi, B. Sundman, Thermo-Calc & DICTRA, computational tools for materials science, Calphad 26 (2002) 273–312.
[56] V.F. Sears, Neutron scattering lengths and cross sections, Neutron News 3 (1992) 26–37.
[57] Y.-J. Zhang, G. Miyamoto, K. Shinbo, T. Furuhara, Quantitative measurements of phase equilibria at migrating α/γ interface and dispersion of VC interphase precipitates: evaluation of driving force for interphase precipitation, Acta Mater 128 (2017) 166–175.

[58] Y. Zhang, G. Miyamoto, K. Shinbo, T. Furuhara, Comparative study of VC, NbC, and TiC interphase precipitation in microalloyed low-carbon steels, Metall. Mater. Trans. A 51 (2020) 6149–6158.

[59] Y.-J. Zhang, G. Miyamoto, K. Shinbo, T. Furuhara, Weak influence of ferrite growth rate and strong influence of driving force on dispersion of VC interphase precipitation in low carbon steels, Acta Mater 186 (2020) 533–544.

[60] D.M. Barnett, On nucleation of coherent precipitates near edge dislocations, Scr. Metall. 5 (1971) 261–266.

[61] A.T. Davenport, R.W.K. Honeycombe, Precipitation of carbides at γ-α boundaries in alloy steels, Proc. R. Soc. Lond. A 322 (1971) 191–205.

[62] H. Dong, Y. Zhang, G. Miyamoto, M. Inomoto, H. Chen, Z. Yang, T. Furuhara, Unraveling the effects of Nb interface segregation on ferrite transformation kinetics in low carbon steels, Acta Mater 215 (2021) 117081.

[63] H. Dong, Y. Zhang, G. Miyamoto, M. Inomoto, W. Zhang, L. Liu, H. Chen, T. Furuhara, Heterogeneous segregation behavior of Nb at the stepped migrating interface during phase transformation, Scr. Mater. 222 (2023) 115038.

[64] H. Dong, Y. Zhang, G. Miyamoto, H. Chen, Z. Yang, T. Furuhara, A comparative study on intrinsic mobility of incoherent and semicoherent interfaces during the austenite to ferrite transformation, Scr. Mater. 188 (2020) 59–63.

[65] M. Kuzmina, M. Herbig, D. Ponge, S. Sandlöbes, D. Raabe, Linear complexions: confined chemical and structural states at dislocations, Science 349 (2015) 1080–1083.

[66] A. Kwiatkowski da Silva, D. Ponge, Z. Peng, G. Inden, Y. Lu, A. Breen, B. Gault, D. Raabe, Phase nucleation through confined spinodal fluctuations at crystal defects evidenced in Fe-Mn alloys, Nat. Commun. 9 (2018) 1137.

[67] A. Kwiatkowski da Silva, I.R. Souza Filho, W. Lu, K.D. Zilnyk, M.F. Hupalo, L. M. Alves, D. Ponge, B. Gault, D. Raabe, A sustainable ultra-high strength Fe18Mn3Ti maraging steel through controlled solute segregation and α-Mn nanoprecipitation, Nat. Commun. 13 (2022) 2330.